Model Based Detection of tubular structures in 3D images

Karl Krissian *, Grégoire Malandain *, Nicholas Ayache * Régis Vaillant ^{o}, Yves Trousset ^{o}

{kkrissia,greg,na}@sophia.inria.fr

* INRIA Sophia Antipolis,

2004, route des Lucioles, B.P. 93,

06902 Sophia Antipolis Cedex (France)

^{o} GEMS

Abstract

Detection of tubular structures in 3D images is an important issue for vascular detection in medical imaging. We present in this paper a new approach for centerline detection and reconstruction of 3D tubular structures. Several models of vessels are introduced for estimating the sensivity of the image second order derivatives according to elliptical cross-section, to curvature of the axis, or to partial volume effects. Our approach uses a multiscale analysis for extracting vessels of different sizes according to the scale. For a given model of vessel, we derive an analytic expression of the relationship between the radius of the structure and the scale at which it is detected. The algorithm gives both centerline extraction and radius estimation of the vessels allowing their reconstruction. The method has been tested on both synthetic and real images, with encouraging results. This work was done in collaboration with GEMS[1].

keywords: filtering, vessel detection, multiscale analysis, segmentation

[1] General Electric Medical Systems, Buc, France

List of symbols

- I_0 initial image,
- t will denote the current scale,
- σ_0 will denote the radius of the initial vessel model which is also the standard deviation of a Gaussian,
- $M(\bar{x})$ will denote a point in the definition domain of the image I_0, $\bar{x} = (x, y, z) \in \mathcal{R}^3$,
- G_{σ_0} Gaussian function with standard deviation σ_0,
- H Hessian Matrix of the image, H' simplified matrix proportional to H,
- $\lambda_1, \lambda_2, \lambda_3$ eigenvalues of the Hessian matrix,
- $\vec{\mathbf{v}}_\mathbf{1}, \vec{\mathbf{v}}_\mathbf{2}, \vec{\mathbf{v}}_\mathbf{3}$ associated eigenvectors,
- $R_t(\bar{x})$ response for a scale t and at a given location $\bar{x}$,
- R_t^n normalized response for a scale t,
- γ normalization parameter;
- t_{max} is the scale at which the normalized response is maximal,
- $L(\bar{x}, t) = I_0(\bar{x}) * G_{\sqrt{t}}$ is the image at a scale t.

1 Introduction

1.1 Motivation

In this paper, we present a new method for segmentation and detection of tubular structures in 3D images. Although the proposed method can be applied to any kind of 3D image, it is especially useful for detection of vascular network in medical images. An accurate detection of the vascular network in medical images fro various organs (liver, lungs, brain) can help physicians in the planning of surgical operations, because the understanding of those 3D images is difficult and the simple visualizations tool are not always sufficient to provide the necessary information.

1.2 Difficulties

Many works exist in the domain of vessel detection applied to 2D images. Yet, the extension of a 2D method to three-dimensional images is not always immediate. The linear structures, which are spaces of co-dimension one in 2D, become spaces of co-dimension 2 in 3D. The definition that we give of a tubular structure will determine the method used for detecting and segmenting it and it will also influence the robustness of the chosen algorithm. Physical reality is complex and the information contained in the image is already a small part of it. On one hand, if we give a **simple** definition of a vessel, the algorithm of detection will be discriminant because it will be able to remove easily the structures which don't correspond to this simple definition. Nevertheless, it will not take into account the complexity of the vessels and it won't be able to detected stenosis, junctions, elliptical cross-sections or high curvatures. On the other hand, if we define a vessel as a **complex** object, willing to take into account its possible defects, we take the risk to detect non-vascular structures. We are faced to this difficulty and it is hard to make a compromise between false positives and false negatives, between the willing to get a complete result and a discriminant one, as long as we try to get a real segmentation of vascular structures.

1.3 Previous works

A way to take into account the varying size of vessels in the image is to apply a multiscale analysis. Multiscale analysis allows to detect structures of various sizes according to the scale at which they give a maximal response. The scale here will be defined by the variance of the Gaussian function with which we convolve the image to compute its derivatives. The response function is a function of the images derivatives.

1.3.1 Linear Scale-Space

When applying a multiscale analysis to an image, the use of the convolution product with a Gaussian kernel and its linear partial derivatives has been shown to be the only way to ensure the following properties: - linearity, - invariance under translation (spatial shift invariance), - invariance under rotation (isotropy), - invariance under rescaling [Koe84, Lin94, FtHRKM92]. Florack et al. [FtHRKM92] show that the evolution through scales can be written using two dimensionless variables L/L_0 and x/σ by the means of the Pi-theorem which states that *a function that relates physical observables must be independent of the choice of dimensional units.*

In his works on scale-space theory [Lin94, Lin96], Lindeberg shows the necessity of normalizing the derivatives of the image in the multiscale analysis. He introduces the notion of γ-normalized derivatives :

$$\partial_{x,\gamma-norm} = t^{\gamma/2}\partial_x \tag{1}$$

When the parameter γ equals one, the normalization ensures invariance under image rescaling, which is compatible with the dimensionless variable $u = x/\sigma$:

$$\frac{\partial I}{\partial u} = \frac{\partial I}{\partial x}\frac{\partial x}{\partial u} = \sigma\frac{\partial I}{\partial x}$$

However, for certain specific task (extraction of 2D blob, of edges, of 2D ridges), Lindeberg studied on analytical models the relationship between the scale at which an object is detected (gives the maximal response), the normalization parameter γ, and the object size, which can lead to choose other values for γ.

In the following, we will implicitly suppose that the scale-space used is linear and obtained from Gaussian convolution of the image and its derivatives.

1.3.2 Medialness

Pizer et al [PBCF94] uses the notion introduced by Blum [Blu67, BN78] in order to characterize the shape of an objet by the means of medial axis containing width information. In 2D images, Blum defined the medial axis as the locus of centers of disks of maximal fit within an object. Making use of the *boundariness* which measures the presence of contours, Pizer et al. define the medial axis, and then the multiscale medial axis (MMA) which defines both the central axis and the width of objects. *Medialness* at a given point and scale $M(x_A, \sigma_A)$ measures the degree of belonging of the point to the medial axis of the object. In [PBCF94], it is defined as the integration over space, scale and direction of a weighted boundariness $W(x_A, x_B, \sigma_A, \sigma_B, u_B)B(x_B, \sigma_B, u_B)$, where the weight W is maximum when - x_B is at a distance from

x_a proportional to σ_B with a constant of proportionality k, - σ_A is proportional to σ_B with a constant of proportionality c, - u_B has the same orientation and direction as $x_B - x_A$.

In a more recent work [PEFM98], he generalized this notion. The medialness can be defined as a convolution product of the initial image with a kernel $K(x, \sigma)$:

$$M(x, \sigma) = I(x) * K(x, \sigma)$$

To ensure the properties of invariance under rotation, translation, and rescaling, K is based on normalized Gaussian derivatives of intensity, computed at a distance from x proportional to σ and at positions that are rotationally invariant relative to x.

He classifies medialness function in two ways: first, central or offset medialness; second, linear or adaptive medialness. On one hand, **central** medialness is obtained by local information, using spatial derivatives of the image at a point x and a scale σ. **Offset** medialness uses the localization of boundaries by averaging spatial information about x over some region whose average radius is proportional to σ. On the other hand, medialness is said to be **linear** when K is radially symmetric and data-independent; and **adaptive** when K is data-dependent.

1.3.3 Ridges of medialness

The different definitions of ridges and their invariance properties where reviewed by Eberly et al. [EGMP94]. They also propose an extension of the concept of ridges of dimension d in n dimensional images:

If $I(\bar{x})$ is a real-valued function defined for $\bar{x} \in \mathcal{R}^n$, and $H(\bar{x})$ is the Hessian matrix of I at $\bar{x}$. Assume that the eigenvalues of $H(\bar{x})$ are ordered as $\lambda_1 \leq \ldots \leq \lambda_n$ with associated eigenvectors $(v_i)_{i \in [1,n]}$, and assume that $1 \leq d \leq n$:

$$\bar{x} \text{ is a ridge point of type } n-d \text{ if and only if } [v_1 \ldots v_d]^t \nabla I(\bar{x}) = 0 \text{ and } \lambda_d < 0.$$

In the context of multiscale analysis, ridges can be extracted in a space including the spatial and scale dimensions. The *Multiscale Medial Axis* [PBCF94, MPL94, FPME94] or also called *core* is an example. Extraction of such ridges requires specific algorithms [Lin96, FEPM95, FP98, PEFM98] as for example the so-called Marching Lines [TG92, TG93] derived from the Marching cubes [LC87] and applied for multiscale crest lines extraction in medical images [Fid97].

1.3.4 Works dedicated to vessel detection

We concentrate here on works using multiscale analysis for vessel detection, especially in 3D, and proposing different response functions (or medialness).

The work of Koller et al [KGSD95] propose a multiscale response in order to detect linear structures in 2D images. The response function uses eigenvectors of the Hessian matrix of the image to define at each point M an orientation orthogonal $\mathcal{D}$ to the axis of a potential vessel that goes through M. From this direction, the response is defined by the minimum of the gradient at two points located at equal distance of M in the direction $\mathcal{D}$. The authors put the emphasis on the discrimination between contours and vessels centers. They propose also en extension to 3D, but without recommending a particular response because in this case, they are not two points equidistant to M but a circle.

Following this work, Lorenz et al [LCBF97] decided to use further information from the Hessian matrix: its eigenvalues. Indeed, after un Taylor expansion to second order of the image intensity Eq. (2), the eigenvalues of the Hessian matrix, when the gradient is weak, express the local variation of the intensity in the direction of the associated eigenvectors.

$$I(M + h\vec{v}) = I(M) + h\,\nabla I\,\vec{v} + \frac{h^2}{2}\vec{v}^{\,t}\,H(I)\,\vec{v} + \mathcal{O}(h^3) \tag{2}$$

In this way, for white structures on dark background, a **linear** structure has two negative and high eigenvalues and a third one which is low in absolute value, and a **planar** structure has only one negative and high eigenvalue and two other low eigenvalues. This noting leads them to define a response function which depend on the eigenvalues of the Hessian matrix. However, the authors show only a single result on a three dimensional image which contains only two tubular structures.

A more recent work done by Sato et al. [SNSA98, SNAK97] also proposes to choose a response function based exclusively on the eigenvalues of the Hessian matrix. The choice of the response function which combines the three eigenvalues is heuristic et is based on an experimental study on various cases (curved vessels, junctions of vessels).

The interest of their work is to show that a single method can given results on several modalities: MRI, MRA, CT and still describing different anatomical structures: vessels in brain, bronchi or liver. Their approach is to provide a visual help in the interpretation of the image after filtering. However, the images used in their experiments seem to have a higher spatial resolution than usual images used in clinical practice, and their algorithm, which uses very few discrete scales, doesn't detect vessel axes and doesn't seem suitable for an accurate estimation of vessel size. In the same state of mind, Frangi et al. [Fra98] propose another response function by interpreting geometrically the eigenvalues of the Hessian matrix.

Using the classification of Pizer et al described in section 1.3.2, all those works present different choices of medialness that are *adaptive* because they depend on the Hessian matrix in a non-symmetric way, and are either *central* [LCBF97, SNSA98, Fra98] or *offset* [KGSD95].

1.4 Contributions and organisation of the article

This paper is based on previous works by the same authors [KMAV98a, KMAV98b, KMA98]. Its contributions are twofold. First, to propose a new adaptive medialness measure for detection of tubular structures in 3D images. The adaptive property of the medialness is based on the characteristics of the Hessian matrix of the image, its eigenvectors and eigenvalues. The analytic study of those characteristics on different models of vessels including elliptical cross-sections and vessel axis curvature show that eigenvectors and gradient are more stable than eigenvectors. This leads us to choose an offset rather than central medialness response. Second, we use a simple model of cylindrical vessel with circular Gaussian cross-section to guide our detection. The analytic computation allows a scale-selection in the same way as Lindeberg [Lin96]. We then express the relationship between the parameters γ,the selected scale, and the structure width and choose those parameters according to the model. From this relationship, we make a full reconstruction of the vessels network.

The first section describes a first cylindrical circular model and two derived models that are curved and with non-circular but elliptical cross-section. Those theoretical models are used to compute eigenvalues and eigenvectors of the Hessian matrix and to interpret their values and their sensitivity with respect to the position of the current point, the image intensity, the radius of the structure, the vessel curvature, the non-circular cross section. The second section describes the proposed measure of medialness, and the automatic scale-selection based on the cylindrical circular model. It also gives the relationship between the size of the structure and its selected scale. Eventually, it explains the extraction of the local extrema and the reconstruction stages. Experiments and results are detailed in a third section. Synthetic images are used to validate the analytical study and to show the behavior of the algorithm under different kinds of tubular structures. An application on real images, that are 3D reconstruction of the brain vessels from 2D X-ray angiographies, is also presented, and the vessel network reconstruction is compared to usual isosurfaces rendering or MIP views.

2 Study of second order derivatives on several models

Following the work of [LCBF97], several articles have been dedicated to the visualization of vessels after a multiscale filtering, whose response is exclusively based on the eigenvalues of the image Hessian Matrix [SNAK97]. In order to understand the link between the eigenvalues and the local structure of the image, we evaluate in this section the analytic expression of these eigenvalues for several theoretical models derived from a simple cylindrical circular model. The cross-section in each model is either a circular or an elliptical Gaussian blob.

In this section, we use the following notations:

- I_0 is the initial image,
- σ_0 denotes the radius of the initial vessel model which is also the standard deviation of a Gaussian,
- G_σ is a Gaussian function with standard deviation σ,
- H is the Hessian Matrix of the image, H' is a simplified matrix proportional to H,
- $\lambda_1, \lambda_2, \lambda_3$ are eigenvalues of the Hessian matrix with $\mid \lambda_1 \mid \geq \mid \lambda_2 \mid \geq \mid \lambda_3 \mid$,
- $\vec{\mathbf{v}}_\mathbf{1}, \vec{\mathbf{v}}_\mathbf{2}, \vec{\mathbf{v}}_\mathbf{3}$ are the associated eigenvectors.

2.1 First model: Cylindrical circular model with Gaussian cross-section

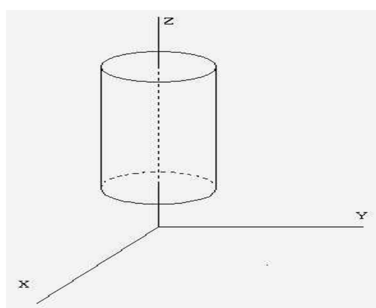

Figure 1: Initial model of a vessel.

The first vessel model that we introduce is cylindrical where (Oz) is the vessel axis and the vessel section is a Gaussian blob:

$$I_0(x, y, z) \; = \; C\, G_{\sigma_0}(x, y) \; = \; \frac{C}{2\pi{\sigma_0}^2} e^{-\frac{x^2+y^2}{2{\sigma_0}^2}}. \tag{3}$$

where C is a function of σ_0 and $\frac{C}{2\pi{\sigma_0}^2}$ represents the intensity at the center of the vessel (Fig. 1). C depends on the size of the vessel, this dependence is due to partial volume effect that decreases the small vessels intensity.

The model properties are:

- the frontier of the vessel is considered to be at the points where the first derivative in the gradient direction is maximum, i.e., for the points which verify $x^2 + y^2 = {\sigma_0}^2$, thus the vessel radius is σ_0.
- if the model is convolved with a Gaussian kernel of standard deviation s, the resulting image is another vessel which matches our model but with a radius $\sqrt{\sigma_0^2 + s^2}$. This result can be directly deduced from the semi-group property.

In order to better take into account the reality of the vessels, we will study two variations of this model. The first one is a toric circular vessel which allows us to introduce a curvature of the vessel. The second one is a cylindrical vessel with an elliptical cross-section which introduces a variation in the circular shape of the vessel.

2.1.1 Expression of eigenvalues and eigenvectors of the Hessian matrix

The Hessian matrix can be expressed as $H = \frac{I_0}{{\sigma_0}^4} H'$ where

$$H' = \begin{bmatrix} x^2 - {\sigma_0}^2 & xy & 0 \\ xy & y^2 - {\sigma_0}^2 & 0 \\ 0 & 0 & 0 \end{bmatrix}$$

and the eigenvalues and eigenvectors of H are

$$\begin{array}{lll} \lambda_3 = 0 & \lambda_2 = -\frac{I_0}{\sigma_0^2}\left[\frac{\sigma_0^2 - (x^2+y^2)}{\sigma_0^2}\right] & \lambda_1 = -\frac{I_0}{\sigma_0^2} \\ \vec{\mathbf{v}}_\mathbf{3} = (0,0,1) & \vec{\mathbf{v}}_\mathbf{2} = (x,y,0) & \vec{\mathbf{v}}_\mathbf{1} = (-y,x,0) \end{array}$$

This means that our model has the following properties:

- Inside the vessel ($x^2 + y^2 < {\sigma_0}^2$) we have two negative eigenvalues with eigenvectors in the plane orthogonal to the axis of the vessel.
- The third eigenvalue is null and the associated eigenvector is in the direction of the axis.
- The eigenvalues λ_1 and λ_2 are maxima in absolute value when $x = y = 0$ and are equal to $-\frac{I_0(x=0,y=0)}{{\sigma_0}^2}$, but λ_2 decreases as a function of the distance to the center.

For the multiscale process, the model is convolved with a Gaussian kernel of standard deviation σ and the results are still valid due to the semi-group property but σ_0 has to be replaced by $\sqrt{\sigma_0^2 + \sigma^2}$.

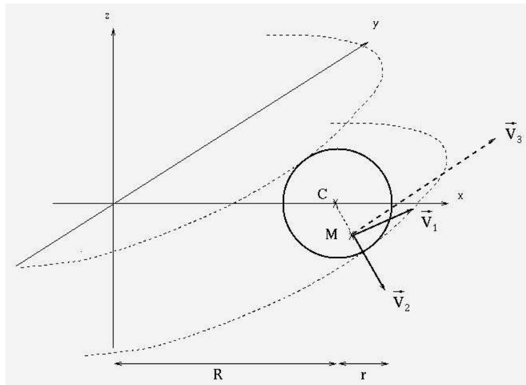

Figure 2: Toric model of a vessel.

2.2 Toric circular model

In this case, the eigenvalues and eigenvectors are similar except that the third eigenvalue is not zero everywhere but only at the center of the vessel (see appendix A).

We modelize the vessel with a torus, the big circle parallel to the plane XY and with a radius R and the small circle with a radius equal to r.

The intensity function of the model is given by the expression:

$$I_0(x, y, z) = Ce^{-\frac{\left(R-\sqrt{x^2+y^2}\right)^2+z^2}{2\sigma_0^2}}.$$

From the circular symmetry around the (Oz) axis, we can choose $y = 0$ and $x > 0$. Then the Hessian matrix H can be expressed as:

$$H = \frac{I_0(x, y, z)}{\sigma_0^4} H'$$

where

$$H' = \begin{bmatrix} (R-x)^2 - \sigma_0^2 & 0 & -z(R-x) \\ 0 & \frac{(R-x)\sigma_0^2}{x} & 0 \\ -z(R-x) & 0 & z^2 - \sigma_0^2 \end{bmatrix}$$

The eigenvectors and eigenvalues of H are (see Fig. 2):

$$\begin{array}{lll} \lambda_3 = -\frac{I_0}{\sigma_0^2}\left[\frac{x-R}{x}\right] & \lambda_2 = -\frac{I_0}{\sigma_0^2}\left[\frac{\sigma_0^2 - CM^2}{\sigma_0^2}\right] & \lambda_1 = -\frac{I_0}{\sigma_0^2} \\ \vec{\mathbf{v}}_3 = (0, 1, 0) & \vec{\mathbf{v}}_2 = (x-R, 0, z) & \vec{\mathbf{v}}_1 = (z, 0, R-x) \end{array}$$

In order to interpret the value of λ_3 depending on the curvature of the vessel $k = \frac{1}{R}$, we center the reference to the center C of the torus in the plane (Ox,Oy). With the new coordinate $x' = x - R$, we have

$$\lambda_3 = -\frac{I_0}{\sigma_0^2}\left[\frac{x'}{R+x'}\right] = -\frac{I_0}{\sigma_0^2}\left[\frac{kx'}{1+kx'}\right].$$

When the curvature is null, $\lambda_3 = 0$ as in the cylindrical case. Nevertheless, this result shows that a vessel curvature can lead to positive ($x > R$) or negative ($x < R$) values of λ_3 in the vicinity of the vessel center.

2.3 Cylindrical elliptical model

The elliptical section is defined by one standard deviation along the x axis, σ_x, and one standard deviation along the y axis, σ_y. The model is thus defined by:

$$I_0(x,y,z) = Ce^{-\frac{1}{2}\left[\left(\frac{x}{\sigma_x}\right)^2+\left(\frac{y}{\sigma_y}\right)^2\right]}.$$

The Hessian matrix can be expressed as

$$H = \frac{I_0(x,y,z)}{\sigma_x^2\sigma_y^2}H'$$

where

$$H' = \begin{bmatrix} \sigma_y^2\left(X^2-1\right) & \sigma_x\sigma_y XY & 0 \\ \sigma_x\sigma_y XY & \sigma_x^2\left(Y^2-1\right) & 0 \\ 0 & 0 & 0 \end{bmatrix} = \begin{bmatrix} E & F & 0 \\ F & G & 0 \\ 0 & 0 & 0 \end{bmatrix}$$

with $X = \frac{x}{\sigma_x}$ and $Y = \frac{y}{\sigma_y}$.

The eigenvalues are (see appendix B for more details):

$$\lambda_1 = \frac{I_0}{2\sigma_x^2\sigma_y^2}(E+G-\sqrt{(E+G)^2+4(F^2-EG)})$$
$$\lambda_2 = \frac{I_0}{2\sigma_x^2\sigma_y^2}(E+G+\sqrt{(E+G)^2+4(F^2-EG)})$$

As $F^2 - EG = \sigma_x^2\sigma_y^2\left[(\frac{x}{\sigma_x})^2 + (\frac{y}{\sigma_y})^2 - 1\right]$, we can distinguish three cases depending on the position of $M(x,y)$, summarized in table 1. We can also study the eigenvalues along the x and y axis. In both cases, if we choose $\sigma_x > \sigma_y$, $\vec{\mathbf{v}}_\mathbf{1} = (0,1,0)$ and $\vec{\mathbf{v}}_\mathbf{2} = (1,0,0)$, table 2 gives the analytic expression of the eigenvalues. Fig. 3 shows the section of an elliptical Gaussian vessel with $\sigma_x = 5$ and $\sigma_y = 3$, and the representation of the eigenvalues $\lambda_1(x,y)$ and $\lambda_2(x,y)$.

Table 1: sign of the eigenvalues at the point M for the elliptical model.

(1)	$(\frac{x}{\sigma_x})^2 + (\frac{y}{\sigma_y})^2 - 1 < 0$	M is *inside* the ellipse,	$\lambda_1 < 0, \ \ \lambda_2 < 0$
(2)	$(\frac{x}{\sigma_x})^2 + (\frac{y}{\sigma_y})^2 - 1 = 0$	M is *on* the ellipse,	$\lambda_1 < 0, \ \ \lambda_2 = 0$
(3)	$(\frac{x}{\sigma_x})^2 + (\frac{y}{\sigma_y})^2 - 1 > 0$	M is *outside* the ellipse,	$\lambda_1 < 0, \ \ \lambda_2 > 0$

Table 2: Expression of eigenvalues along x and y axis for the elliptical model.

x axis (y = 0)	$\lambda_1 = -\frac{I_0}{\sigma_y^2}\left(1 - \frac{y^2}{\sigma_y^2}\right)$	$\lambda_2 = -\frac{I_0}{\sigma_x^2}$
y axis (x = 0)	$\lambda_1 = -\frac{I_0}{\sigma_y^2}$	$\lambda_2 = -\frac{I_0}{\sigma_x^2}\left(1 - \frac{x^2}{\sigma_x^2}\right)$
center (x = y = 0)	$\lambda_1 = -\frac{I_0}{\sigma_y^2}$	$\lambda_2 = -\frac{I_0}{\sigma_x^2}$

The eigenvectors are:

$$\vec{\mathbf{v}}_i = \begin{pmatrix} \lambda_i - G \\ F \\ 0 \end{pmatrix} = \begin{pmatrix} F \\ \lambda_i - E \\ 0 \end{pmatrix} \quad \text{for} \ \ i \in \{1, 2\}.$$

Fig. 4 shows the curves which are tangent to the eigenvectors at each point of a section of the vessel.

At the center of the center of the elliptical vessel, one interesting property is that the ratio of the two main eigenvalues is equal to the inverse of the square of the ratio of the respectives radii:

$$\frac{\lambda_1}{\lambda_2} = \left(\frac{\sigma_x}{\sigma_y}\right)^2$$

This means that a given variation on the radii ratio will lead to a higher variation of the eigenvalues ratio.

2.3.1 Conclusion about the eigenvalues of the Hessian matrix

In the three models studied, we have at the center of the vessel one eigenvalue which is zero with the corresponding eigenvector in the direction of the axis of the vessel, and the two other eigenvalues are negative and equal if the section is circular, or approximatively equal if the section is an ellipse with $\sigma_x \approx \sigma_y$. The relations of (**??**) can be replaced by (4) which are more restrictive but σ_0 is unknown and the criteria remain qualitative:

$$\frac{-\lambda_1({\sigma_0}^2 + t)}{G_{\sqrt{t}} * I_0} \approx 1 \text{ and } \quad \lambda_1/\lambda_2 \approx 1 \text{ and } \quad \lambda_1 \gg \lambda_3. \tag{4}$$

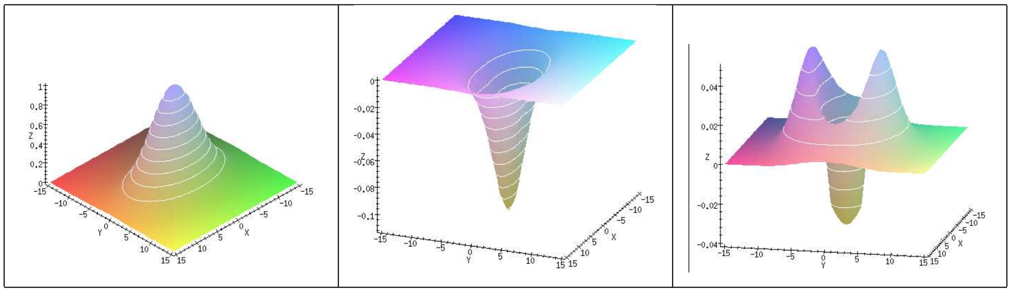

Figure 3: Left to right, surface of the Gaussian ellipse with $\sigma_x = 5$ and $\sigma_y = 3$, surface $z = \lambda_1(x, y)$, and surface $z = \lambda_2(x, y)$.

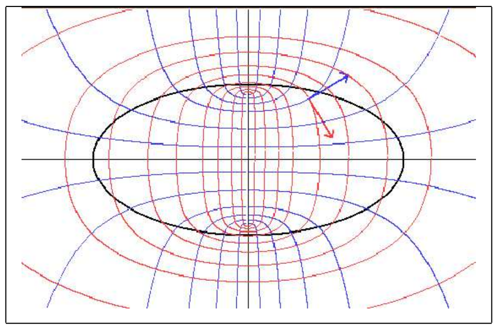

Figure 4: Representation of the curves which are tangent to the eigenvectors. In red, the curves tangent to $\vec{\mathbf{v_1}}$ and in blue the curves tangent to $\vec{\mathbf{v_2}}$.

The first of this equality comes from the relation $\lambda_1 = -I_0/\sigma_0^2$, where at a given scale, I_0 must be replaced by its convolution with a Gaussian $G_{\sqrt{t}}$ and σ_0^2 must be replaced by $\sigma_0^2 + t$. Furthermore, vessels sizes are usually thinner than two or three voxels and the eigenvalues are not computed at the real vessel center but at the center of a voxel. Thus, the models presented above emphasize the difficulty in relying on eigenvalues of the Hessian matrix for an accurate detection of vessel center and size. In particular, the relationship $\lambda_1/\lambda_2 \approx 1$ is difficult to obtain in real images. For this reason, we propose to use eigenvalues of the Hessian matrix for the discrimination of vessel-like structures from other structures, and to use a gradient-based response function for the extraction of the vessel centerlines.

3 The method

Our approach can be split into three steps. We first compute the multiscale response $R_{multi}(I_0)$ from responses at a discrete set of scales, we then extract the local extrema R^e_{multi} in $R_{multi}(I_0)$, and finally we create a skeleton of R^e_{multi} and visualize the results. Vessels are also reconstructed using both the centerlines and the size information. In the first step, we use a model of the vessels both for interpreting the eigenvalues and the eigenvectors of the Hessian matrix and for choosing a good normalization parameter.

Computation of the *single scale response* requires different steps. First, a number of points are pre-selected using the eigenvalues of the Hessian matrix. These points must be near a vessel axis. Then, for each pre-selected point, the response is computed at the current scale. The response function uses information from both eigenvectors of the Hessian matrix and gradient vectors located on a circle centered on the current point. Finally, this response is normalized in order to give a multiscale scale response that combines interesting features of each single scale response. These steps are detailed in the following paragraphs.

The following notations are used:

- t denotes the current scale,
- $M(\bar{x})$ denotes a point in the definition domain of the image I_0, $\bar{x} = (x, y, z) \in \mathcal{R}^3$,
- $R_t(\bar{x})$ is the response for a scale t and at a given location $\bar{x}$,
- R^n_t is the normalized response for a scale t,
- γ is a normalization parameter,
- t_{max} is the scale at which the normalized response is maximal,
- $L(\bar{x}, t) = I_0(\bar{x}) * G_{\sqrt{t}}$ is the image at a scale t.

3.1 Pre-selection of candidates using eigenvalues of the Hessian matrix

In order to compute the response at one scale R_t, we need a pre-selection of the points that are near the vessel axis, and also a good estimation of the vectors $\vec{\mathbf{v}}_\mathbf{1}$ and $\vec{\mathbf{v}}_\mathbf{2}$ that give an orthogonal basis in the plane of a section. This pre-selection is both a discrimination of potential tubular structures and a way to save computation time.

For this pre-selection, we use a weak version of the criteria given in Eq. (4) where we only test that λ_1 and λ_2 are negative. We can afford to make this weak discrimination because the only structures of high intensity present in the studied images are vessels. An extension of our approach for other modalities would require the choice of some thresholds for each of the three approximations given in Eq. (4).

3.2 Computation of the response R_t at one scale t

A first choice for R_t can be a 3D extension of the 2D response proposed by Koller et al. [KGSD95]. For a point x, the response is set to the minimum of the absolute value of the intensity's first order derivative computed at 4 points equidistant from x. An advantage of this choice is to ensure that a high response results in a high probability of being at a vessel's center, but this medialness response is too sensitive to noise. It seems more natural to use information from the first derivative at every point of a circle than just four points. This circle $C(M,t)$ is centered at the current point $M(\bar{x})$, has a radius $\theta\sqrt{t}$, and is parallel to the eigenvectors $\vec{\mathbf{v_1}}$ and $\vec{\mathbf{v_2}}$. The proportionality constant θ will be chosen according to the model. This constant is the inverse of the constant $\rho = \frac{1}{\theta}$ already introduced in [PEFM98]. We will see in section 3.3.3 how this constant can be chosen to optimize the response at the maximal scale.

We propose to use the following medialness response:

$$R_t(\bar{x}) \;=\; \frac{1}{2\pi}\int_{\alpha=0}^{2\pi} -\nabla_t I_0\left(\bar{x} + \theta\sqrt{t}\,\vec{\mathbf{v}}_\alpha\right).\vec{\mathbf{v}}_\alpha d\alpha \tag{5}$$

with $\vec{\mathbf{v}}_\alpha = cos(\alpha)\vec{\mathbf{v}}_\mathbf{1} + sin(\alpha)\vec{\mathbf{v}}_\mathbf{2}$. This response is the mean of first order derivative information taken at the circle $C(M,t)$. $\vec{\mathbf{v}}_\alpha$ is the radial direction and $\nabla_t I_0$ is the gradient vector of the initial image, computed at the scale t. To ensure a positive response for white structure on dark background, we take the opposite of the scalar product between the gradient and the radial direction.

In practice, we must compute this response for a discrete image. Thus, we use $N = E(2\pi\sqrt{t}+1)$ points along the circle $C(M,t)$, where $\forall n \in \mathcal{R}, E(n)$ is the integer part of n, it leads to the discrete formulation:

$$R_t(\bar{x}) \;=\; \frac{1}{N}\sum_{i=0}^{N-1} -\nabla_t I_0\left(\bar{x} + \theta\sqrt{t}\,\vec{\mathbf{v}}_\alpha\right).\vec{\mathbf{v}}_\alpha, \quad \text{with} \;\; \alpha = 2\pi i/N. \tag{6}$$

The value of the gradient vector at the point $\bar{x} + \theta\sqrt{t}\vec{\mathbf{v}}_\alpha$ is obtained by trilinear interpolation of the gradient vector, allowing a better boundary estimation.

3.3 Normalization

3.3.1 Normalization: analytic study

One difficulty with multiscale approach is that we want to compare the result of a response function at different scales while the intensity and its derivatives are decreasing functions of scale. Lindeberg [Lin94, Lin96] introduced the notion of normalized derivatives in order to deal with this problem. If the scale t is defined as $t = \sigma^2$ where σ is the standard deviation of the Gaussian, the $\gamma-$**normalized derivative** ∂_γ was already defined by Eq. 1.

The value of γ is chosen to allow the response R_t to be maximal for a scale corresponding to the size of the structure we want to detect. In practice, we need a structure model in order to estimate the value of γ. At a scale t, the cylindrical circular model with a constant $C > 0$ leads to

$$L(\bar{x}, t) = I_0(\bar{x}) * G_{\sqrt{t}}(\bar{x}) = CG_{\sqrt{\sigma_0^2+t}}(\bar{x}).$$

Appendix C gives some details about the calculation of the maximum of the normalized response R_t^n:

$$R_t^n \;=\; C\frac{\theta t^{\frac{\gamma+1}{2}}}{2\pi\,(t+\sigma_0^2)^2}\, e^{-\frac{\theta^2 t}{2(t+\sigma_0^2)}} \tag{7}$$

We find a relation of proportionality between the scale t_{max} that gives a maximal response and the initial radius of the vessel σ_0:

$$t_{max} \;=\; h(\gamma,\theta)\sigma_0^2 \tag{8}$$

where h is a function of the normalization parameter γ and the proportionality constant θ:

$$h(\gamma,\theta) = \frac{\sqrt{\Delta} - 2\gamma + 2 - \theta^2}{2(3-\gamma)} \quad \text{with} \;\; \Delta = \left[\theta^2 - (2\gamma-2)\right]^2 + 16 - (2\gamma-2)^2 \tag{9}$$

3.3.2 Zoom-invariant criterion

If we take into account the fact that several vessels of various radii interact with each other, another criterion for normalization is to choose γ so that the maximum response at the center of a vessel doesn't depend on the size of this vessel. This choice will avoid privileging vessels of certain radii in the multiscale integration. For example, if the maximum response at the center of a big vessel is higher than the maximum response at the center of a small vessel, and the two vessels are neighbours, the big vessel may create side effects which will disturb the extraction of the small vessel in the multiscale integration. Moreover, finding a single threshold to extract the centerlines of all vessels in the final image will be more difficult.

This normalization requires choosing a realistic value for $C(\sigma_0)$ in the current model. If we choose the constant $C = 1$, the intensity at the center of a vessel will decrease when the radius σ_0 increases. A first approximation is that the intensity at the center of the vessel doesn't depend on its size, which leads to the constant $C = 2\pi\sigma_0^2$. Then, the intensity of a vessel will be equal to

$$I_0(x,y,z) = 2\pi\sigma_0^2 G_{\sigma_0}(x,y) = e^{-\frac{x^2+y^2}{2\sigma_0^2}}.$$

As $2\pi\sigma_0^2$ doesn't depend on scale or space, previous results are still valid. Thus, we choose the value 1 for γ. This value ensures a nice behaviour under spatial rescalings of original image, defined as the *scaling property* in [Lin94].

3.3.3 Choice of the constant θ

The purpose of introducing the parameter θ is to compute the boundariness at a distance which is equal to the frontier of the vessel at the maximal scale t_{max}. This can be achieved for our vessel model. At a given scale t, the frontier of the vessel is at a distance $\sqrt{\sigma_0^2 + t}$ from the vessel center. As the response uses information of the gradient at a distance $\theta\sqrt{t}$, we would like to have the following relation

$$\theta\sqrt{t_{max}} = \sqrt{\sigma_0^2 + t_{max}}$$

Introducing Eq. (8) and having set γ to the value 1, we find a solution to this relation given by $\theta = \sqrt{3}$.

Once we have chosen the two parameters γ and θ, two numerical relations can be deduced for our vessel model. The first one is proportional relation between the size of the vessel and the scale at which it is detected $t_{max} = h(\gamma, \theta)\sigma_0^2 = 0.5\sigma_0^2$. The second one is the value of the maximal response $R^n_{t_{max}}$ when the intensity of the vessel center is set to 1 ($C = 2\pi\sigma_0^2$):

$$R^n_{t_{max}} = \sigma_0^{\gamma-1} \frac{\theta\, h(\gamma,\theta)^{\frac{\gamma+1}{2}}}{(h(\gamma,\theta)+1)^2} e^{-\frac{\theta^2 h(\gamma)}{2(h(\gamma)+1)}} = 2\sqrt{3}/9e^{-1/2} \approx 0.233 \tag{10}$$

In practice, for each acquisition modality, a statistical study must be done to estimate the relation between the intensity at the center of a vessel and the radius of this vessel, and the response should be normalized according to this relation.

3.4 Computation of the multiscale response

The multiscale response is defined as the maximum of response set taken at different scales. The scales are discretized from t_l to t_h using a logarithmic scale in order to have more precision at low scales where the standard deviation is smaller and where we want to detect smaller structures. Fig. 5 shows Maximum intensity Projections (MIP views) of the normalized responses of an image. Six scales were used for radii of vessels ranging from 1.0 to 3.5: {1.0, 1.28, 1.65, 2.12, 2.72, 3.5}. If r is the radius of the vessel we want to detect, the associate scale chosen for the detection is $h(\gamma)r^2$.

A MIP view of the initial image is shown at the top left of Fig. 6, and a MIP view of the multiscale response which is the maximum response across the set of scales is shown beside.

3.5 Extraction of local maxima in $R_{multi}(I_0)$

Our definition of local extrema in $R_{multi}(I_0)$ is a special case of the *Height ridge* definition [FKMP97]. Some recent work [FPE96, Lin96, Fid97] in ridge extraction use the "Marching Lines" algorithm [LC87, TG93].

For each spatial point $M(x, y, z) \in \mathcal{R}^3$, we associate the *scale-space point* $M^t(x, y, z; t) \in \mathcal{R}^3 \times \mathcal{R}_+$ where $t = t_{max}(M)$ is the scale at which the response at M is maximal (we suppose that this scale is unique which is the case for our model). We also define $\vec{\mathbf{t}}$ as a vector in the scale direction.
We define a local maximum in the scale-space normalized response $R_t^n(\bar{x})$ as a point $(\bar{x}; t) \in \mathcal{R}^3 \times \mathcal{R}_+$ which is locally maximal in the directions of $\vec{\mathbf{v_1}}(\bar{x}; t)$, $\vec{\mathbf{v_2}}(\bar{x}; t)$ and $\vec{\mathbf{t}}$. We can easily state that for every central point M of a vessel, its associated scale-space point M^t is locally maximal in the scale-space response. If the converse is true, i.e. all the local maxima in the scale-space response are located at central points of a vessel, then detecting the centerlines is equivalent to extracting those local maxima. This assumption can be verified in the vicinity of the central points. This vicinity is obtained by pre-selection of candidates (paragraph 3.1).

In practice, we use Eq. (11) as a characterization of the local extrema.

$$
\begin{aligned}
(\bar{x}; t_i) \text{ is locally maximal} \quad \Longleftrightarrow \quad & R_{t_i}^n(\bar{x}) \geq R_{t_i}^n(\bar{x} \pm \vec{\mathbf{v_1}}) \text{ and } R_{t_i}^n(\bar{x}) \geq R_{t_i}^n(\bar{x} \pm \vec{\mathbf{v_2}}) \\
& \text{and } R_{t_i}^n(\bar{x}) \geq R_{t_{i\pm 1}}^n(\bar{x}) \qquad (11)
\end{aligned}
$$

A MIP view of an image of the local extrema is shown at the bottom left of Fig. 6.

3.6 Skeletonization, reconstruction and visualization

It is not an easy task to visualize the local extrema image in order to improve the interpretation of the original data image. For that purpose, we propose to extract some information from the local extrema image, to superimpose it into some 3D representation of the original data image (volume or surface rendering) or to use it for a vessel network reconstruction.

Skeletonization. *First*, we binarize the local extrema image by applying a hysteresis thresholding, with manually chosen thresholds. *Second*, we thin this result to obtain a skeleton-like representation of the vessels. Thinning is achieved by deleting the simple points. These points are the ones whose removal does not change the topology of the image. More details of the skeletonization algorithm can be found in [BM94]. The resulting skeleton is composed of pieces of curves, each of them representing a piece of vessel. *Third*, the skeleton is simplified by removing small pieces of curves. For a better visualization, the remaining curves are smoothed using an energy minimization including data attachment. The smoothing method is derived from [Del94] and doesn't modify the localization of the extremities of each line. The result obtained is an image of the vessel axes.

Reconstruction. The centerline image also contains information about the size of the vessel, which is proportional to the scale at which the current point has been extracted. The relation between a vessel size and the scale at which it was detected was given in paragraph 3.3.2. The bottom right image of Fig. 6 represents a MIP view of the centerlines obtained, where central points are colored according to the scale at which they have been extracted, six colors are used ranging from blue to red for the six single-scale responses shown in Fig. 5.

Each piece of vessel is described by a sequence of points $\{c_i\}$, each of them being associated with an estimated radius r_i. We reconstruct each segment $[c_i, c_{i+1}]$ independently. If the orthogonal projection c of a point M on the line $c_i c_{i+1}$ is into the segment $[c_i, c_{i+1}]$, we estimate the radius in c, and deduce from it the intensity in M with Eq. (3). This way, we reconstruct a grey-level image and we visualize easily all the reconstructed vessels with an isosurface.

Visualization. The usual means of visualizing the vessel network are not effective.

On the one hand, MIP views can mislead the physicians because they don't contain information about the relative position of the vessels in depth. One can add depth-cueing to them but a high intensity vessel located behind a low intensity vessel may still appear to be in front of it, or hide it.

On the other hand, an isosurface of the initial image can account for the the *relative position* of the vessels, but it contains *partial information* about the image which is insufficient. With a low threshold an isosurface contains the small vessels but they are hidden by the big vessels. With a high threshold, it contains only the thickest vessels as shown in Fig. **??**.

In both cases, MIP view or isosurface, the superimposition of the detected 3D centerlines can help the interpretation of the real vessel network. Moreover, an isosurface of the reconstructed vessel network have the advantages of an initial image isosurface without having its drawbacks, because all vessels are reconstructed with the same centerline intensity. Thus, it can help to understand the local structure of the vessels network.

4 Experiments and Results

4.1 Experimental study on synthetic images

In this section, we present some experiments made on synthetic images. The purpose is to estimate the sensitiveness and to understand the limits of our method on several criteria: normalization, radius estimation, curvature, tangency of vessels, junctions. The created images have a Gaussian blob cross-section and their difference from the theoretical models lies in their discrete representation. This choice allows to check the expected results found by the analytic study. However, we also compare the response profile obtained for *bar-like* and *Gaussian-like* cross-sections on a cylindrical circular model.

This study on synthetic images is not exhaustive, but we hope that it leads to a better understanding of problems arising in vessels segmentation. In the ideal case, the spirit of the work on synthetic images is to *first* find all the difficulties; *second* create synthetic image that isolate each difficulty, understand the behavior of the method on this problem and try to improve it; *third* expect that a single algorithm which handles each of these difficulties separately will give good results on real images.

4.1.1 Cylindrical circular vessels with Gaussian cross-section

Response profile The response profile is the evolution of the medialness response as a function of scale, here taken at the vessel center. Figure 7 shows a comparison between the theoretical and the obtained profiles. The synthetic image contains a circular cylinder with Gaussian blob cross-section, radius 3 voxels and intensity equal to 100 at the center. The theoretical response profile is given by Eq. (7) where $\sigma_0 = 3$, $\gamma = 1$, $\theta = \sqrt{3}$ and $C = 2\pi\sigma_0^2 \times 100$. The experimental response profile is obtained from twenty scales ranging from 0.7 to 3.5. This comparison shows that the two profiles match, and that the experimental profile is slightly lower than the theoretical one near the maximal scale.

Normalization The relationship between the vessel radius and the optimal scale is $t_{max} = h(\gamma, \theta)s_0^2 = 0.5s_0^2$ where s_0 is the radius of the vessel with Gaussian-like cross-section. The response at the optimal scale and at the vessel center should be zoom invariant and equal to ≈ 0.23345 times the intensity at the vessel center (according to Eq. (10)). The initial image of Fig. 8 contains four vessels with Gaussian blob cross-section and respective radii: 1.25, 1.75, 2.5, 3.5.

After applying the multiscale analysis on this image with 20 scales for vessels radii ranging from 1 to 4 voxels, the second row of Table 3 presents the maximum intensity obtained at the center of each vessel. The distance to the theoretical value of the maximum is stronger for small vessels and is probably due to the trilinear interpolation of the gradient vector during the response computation. This distance remains small , below 11%, which confirms the zoom invariant property of the normalization, and will allow an easy threshold of the local extrema image (Fig. 8).

Radius estimation Rows 3 and 5 of Table 3 show radius estimation for the same image. Except for the vessel of size 1.25, the maximum response is obtained at the nearest scale associated to the size of the vessel. The error in size estimation is below 0.3 voxel and improves when the vessel size increases. This result shows that, due to discretization, we cannot hope to get an accurate sub-voxel estimation of the size of small vessels, i.e. vessels of radius below 1.5 voxels.

Other cross-section models These first tests set the problem of sensitiveness to the cross-section model. In real images, there should not be high intensity variations inside the vessel. Two main reasons of intensity variation can be noise and partial volume effect. Concerning noise, the multiscale process that uses Gaussian kernel convolutions tends to reduce it, but depending on the acquisition modality, one can apply a pre-filtering technique like anisotropic diffusion. The partial volume effect disturbs the detection of small vessels and also reduce their intensity. In fact, big vessels can be considered as having a *bar-like* cross-section whereas small one have a *Gaussian-like* cross-section and a lower intensity caused by partial volume effect.

Fig. 9 shows response profiles for different cross-sections on a cylindrical circular vessel of radius 3. In red, the profile for a Gaussian-like cross-section, the same as in Fig. 7, and in blue the response profile for a bar-like cross-section. There are important variations between those two profiles, bar-like cross-section have they maximum with a higher response value and at a lower scale. This result shows that our vessel size estimation can not be accurate without having a good model of the vessel cross-section.

We are currently working on a vessel model of a bar-like cross-section convolved with Gaussian kernel with a constant and small standard deviation. In this cross-section model, the Gaussian kernel convolution acts like a partial volume effect and can lower the intensity of small vessel: big vessels are "bar-like" and small ones are "Gaussian-like". Using this kind of model closer to real images, size estimation can be considerably improved. Fig. 9 shows in green the profile response obtained for a bar-like cross-section of radius three and convolved with a Gaussian kernel of standard deviation 1, and in red the profile using a standard deviation equal to the vessel radius (3).

Although the size estimation is not accurate for non-Gaussian cross-section, it can give a good idea of the size variation in the whole vessels networks and the relatives radii between different vessels. Then, our result after reconstruction can also give a good initialization for a more precise boundary detection using region-growing methods or level sets.

4.1.2 One vessel with varying width

Fig. 10 and Fig. 11 show experiments made on vessels with varying width. The vessel size of the images is a periodic sinusoid and the radius varies from 2 to 4 voxels with a period of $zsize/n$ voxels $n \in [1, 2, 4]$ and $zsize = 100$, along z axis. The equation of the vessel radius for $n = 1, 2, 4$ is :

$$R(z) = 4 + 2sin(2\pi n \frac{z}{zsize}))$$

The local extrema in Fig. 10 shows that the vessel center has been well detected and also that some extrema were detected near the vessel frontiers when the radius goes though a maximum. In this case, there are two negative eigenvalues in the plane tangent to the vessel contour, and it is normal to obtain local extrema. Nevertheless, the response obtained at the vessel center is higher and the *false* responses can be removed either by thresholding of the image of local extrema or by removal of small connected components.

Fig. 11 shows the estimated radius (in red) along z axis compared to the real radius profile of the vessel (in blue). For smooth variations, on the left, the size is well estimated, but for fast variations of radius, on the right, in regions of maximum radius the size is under-estimated due to the Gaussian convolution at high scales that decreases the intensity near those frontiers, faster than in the cylindrical case.

4.1.3 Curved vessels

For a single torus with a Gaussian cross-section, the local extrema gives high response at the torus center where the intensity is higher than 18.00 and some response near the outside frontier of the torus. This second type of response is explained by the negative value of the third eigenvalue that becomes higher in absolute value than the second one (see section 2.2). However, it has an intensity lower than 9.0 and can easily be threshold. Fig. 12 right shows the threshold extrema superimposed on the initial image. The location of the vessel center doesn't have a sub-voxel precision, but the voxels found for the vessel center contain the real vessel center independently of the curvature (bottom row of Fig. 12).

4.1.4 Tangent vessels

We say that two vessels are tangent when their frontiers are enough near to disturb the estimation of the gradient. Generally, the tangency concerns two vessels but in some cases more vessels can be involved, or a vessel can be tangent to a non-vessel structure. We restrict the study to the case of two vessels.

The tangency can be characterize by three parameters: 1) the minimal distance d between the two vessels frontiers compared to the size of the vessels; 2) the ratio between the two vessels radii; 3) the angle $\alpha \in [0, \pi/2]$ between the two vessels axis at the tangent locus.

In our experiments, we set the ratio of the two vessels to 1 (their radius is three voxels) and tested the cases $\alpha = 0$ in Fig. 13 and $\alpha = \pi/2$ in Fig. 14.

Fig. 13 shows results on the first case $\alpha = 0$ where the distance d is equal to zero on the right and to the vessel radius i.e. three voxels on the left. When $d = 0$, a third line is detected between the two vessels and at a higher scale (bottom right), while the continuities of the two vessels centerlines are preserved. As the detected lines are not connected, it is possible to remove the "wrong" line by removing small connected components, but not by thresholding the local extrema image. On the bottom left image, the distance between the two vessels is equal to their radius and a thresholding of the local extrema image is sufficient for removing the “wrong” detected local extrema.

Fig. 14 shows results for $\alpha = \pi/2$, where the distance d decreases from 4 voxels to 0. In this case, there is no third line created by the tangency, but the disturbance on the centerline position is more important. This important displacement of the vessel center for a vessel denoted v_1 at the right of Fig. 14 can be explain by the low curvature of the tangent surface of the other vessel v_2 in the direction orthogonal to v_1. This low curvature, equal to zero here, disturb the medialness response which integrate boundariness along a circle orthogonal to v_1 axis.

In the same way, when a small vessel is tangent to a “bigger” one, we can expect disturbance in the small vessel axis detection due to the low curvature of the big vessel, even when vessels are parallel i.e. for low values of α.

As a conclusion, when the boundaries of tangent vessels are not in contact, one can expect to keep the continuity of the vessels centers. Nevertheless, tangency of vessels have the following negative effects: - it decreases the response function and makes the thresholding more difficult, - it increases the estimated size of the vessel near the tangent area, - it changes the location of centerlines. One way to improve the detection of tangent vessels can be to make an iterative process. The information of the detected vessels can be used to localize the region of tangency and to discard the information of gradient in those regions for the next iteration.

4.1.5 Junctions

A junction in a vessels network is a branching of vessel, where one vessel divides into several branches, in general two. We restrict this experimental study to the case of two branches.

Fig. 15 shows experiments made on three synthetic junction images. The centerlines detection, obtained from the extraction of local maxima of the multiscale response, does not ensure the continuity of the junction detection. In the top image, the main vessel divides into two branches of the same size and the continuity is preserved, but in the middle and in the bottom image, the two branches don’t have the same size and the junction continuity is not preserved by the centerlines. This discontinuity can still be present after the reconstruction (middle image).

To solve this problem, the junctions can be connected using the centerlines and the radii information. Assuming that the bigger vessel keeps its continuity, a junction is restored when the distance between extremity E of a vessel v_1 and the axis of second vessel v_2 is lower than the radius of v_2:

$$d(E, v_2) < r(v_2) * \alpha + \beta \tag{12}$$

where α stands for the error in radius estimation and β is the sum of the error in the location of v_2 axis and in the location of the extremity E of v_1. To perform the junction connection, each extremity E of a vessel v_1 is projected on every segment of every vessel different from v_1 and located in the vicinity of E, and d is the distance to the nearest projected point P. We set $\alpha = 1.2$ and $\beta = 2$ voxels. Fig. 15 shows the restored centerlines and the reconstruction from those centerlines for two junction images.

4.2 Real Images

4.2.1 Brain Vessels from X-ray images

Image Acquisition Our algorithm was tested on a set of images produced by General Electric Medical Systems, Buc, France. They are obtained by 3D reconstruction of the vessels from 2D X-ray substracted angiographies. Details of the reconstruction scheme can be found in [Pay96]. Compared to the other 3D acquisition modalities which are Magnetic Resonance Angiography and Scanner Angiography, this 3D reconstruction gives a high isotropic resolution over the whole reconstructed volume. However, it requires a good opacification of the vascular network obtained with an intra-arterial injection. The left images in Fig. 16 are MIP views of a typical sub-images centered on an aneurysm. They contain different artefacts: noise, partial volume effect, consequences of the patient motion between different acquisitions and 3D reconstruction artefacts which lead to a non-homogeneity of the intensity of the vessels for different sizes of the vessel. The two right columns of Fig. 16 show isosurfaces of the images, where small vessels are only visible with a low threshold (surface holes in black are due to the image boundaries).

Results We tested our algorithm on ten images $128 \times 128 \times 128$ of varying comlexity. Because small vessels have an lower intensity than bigger ones, we used a parameter γ slightly lower than 1 for the normalization. Decreasing the value of γ has the effect of enhancing small vessels compared to big ones, and helps to compensate for intensity variations. Empirically, we found that 0.75 gave good results. The minimum and maximum scales are chosen according to the radius of the thinnest and the thickest vessels in the initial image. The algorithm was run with eight scales ranging from 0.5 to 4. The time used for computing the response of the extrema was 7 minutes with an AlphaStation 500, 400 MHz. Then, after manual thresholding for binarization, the skeletonization and the smoothing of the centerlines take a few seconds.

The results on three images are shown in Fig. 17.

Each of these figures shows on the left column the MIP of the initial image and the detected centerlines; and on the right column the comparison between isosurfaces of the initial image and the reconstructed vessels network The following interesting points are emphasized: Continuity of junction (letters J), continuity and good detection of tangent vessels (letters T), detection and enhancement of vessels with low intensity and hard to visualize in MIPs or isosurfaces (letters E).

4.2.2 Brain Vessels from MRA

5 Conclusion and future work

We introduced a model of 3D vessels which allows us to choose several parameters of the multiscale detection. The advantages of this model based detection is *first* to better understand the pre-selection of central points according to the Hessian matrix eigenvalues, *second* to find a good normalization, and to know the exact relation between the scale at which the response is maximal and the size of the vessel (Eq. (**??**)). The algorithm has already a good behavior and promising results, but some local problems occurring at junctions or tangent vessels have to be studied more thoroughly. Finally, we plan to use our method with other acquisition modalities such as Magnetic Resonance Angiography or CT images, and to use also the vessel information to help in the detection and the segmentation of aneurysms.

Acknowledgements
The authors want to acknowledge the contributions of Yves Trousset and Rgis Vaillant from GEMSE, Buc, France. This work was funded in part by GEMS (General Electric Medical Systems).

A Eigenvalues for a toric model with circular section

If we modelize the vessel with a torus, the big circle parallel to the plane XY and with a radius R and the small circle with a radius equal to r.

The square distance from a given point $M(x, y, z)$ to the axis of the torus is given by:

$$\left(R - \sqrt{x^2 + y^2}\right)^2 + z^2$$

derived from the cylindrical model, we can take the following function of intensity:

$$I_0(x, y, z) \;=\; Ce^{-\frac{\left(R-\sqrt{x^2+y^2}\right)^2+z^2}{2\sigma_0^2}}$$

The first and second derivatives are:

$$\frac{\partial I_0}{\partial x} \;=\; \frac{I_0 x}{\sigma_0^2}\left(\frac{R}{\sqrt{x^2+y^2}} - 1\right)$$

$$\frac{\partial^2 I_0}{\partial x \partial y} = \frac{I_0 xy}{\sigma_0^2}\left[\frac{1}{\sigma_0^2}\left(\frac{R}{\sqrt{x^2+y^2}} - 1\right)^2 - \frac{R}{(x^2+y^2)^{\frac{3}{2}}}\right]$$

$$\frac{\partial^2 I_0}{\partial x^2} = \frac{I_0 x^2}{\sigma_0^4}\left(\frac{R}{\sqrt{x^2+y^2}} - 1\right)^2 + \frac{I_0}{\sigma_0^2}\left[\frac{Ry^2}{(x^2+y^2)^{\frac{3}{2}}} - 1\right]$$

$$\frac{\partial^2 I_0}{\partial z^2} = \frac{I_0}{\sigma_0^4}(z^2 - \sigma_0^2)$$

$$\frac{\partial^2 I_0}{\partial x \partial z} = -\frac{I_0 xz}{\sigma_0^4}\left(\frac{R}{\sqrt{x^2+y^2}} - 1\right)$$

From the circular symmetry around Oz axis we can choose $y = 0$ and $x > 0$, then the Hessian can be expressed as:

$$H = \frac{I_0(x, y, z)}{\sigma_0^4} H'$$

where

$$H' = \begin{bmatrix} (R-x)^2 - \sigma_0^2 & 0 & -z(R-x) \\ 0 & \frac{(R-x)\sigma_0^2}{x} & 0 \\ -z(R-x) & 0 & z^2 - \sigma_0^2 \end{bmatrix}$$

The determinant of $H' - \lambda Id$ is:

$$det = \left[\frac{(R-x)\sigma_0^2}{x} - \lambda\right]\left[\lambda - \left((R-x)^2 + z^2 - \sigma_0^2\right)\right]\left[\lambda + \sigma_0^2\right]$$

and the eigenvalues of H' are:

$$\begin{array}{ll} \lambda_3 = \frac{(R-x)\sigma_0^2}{x} & \vec{\mathbf{v}}_\mathbf{3} = (0, 1, 0) \\ \lambda_2 = (R-x)^2 + z^2 - \sigma_0^2 & \vec{\mathbf{v}}_\mathbf{2} = (x - R, 0, z) \\ \lambda_1 = -\sigma_0^2 & \vec{\mathbf{v}}_\mathbf{1} = (z, 0, R - x) \end{array}$$

and the eigenvalues of H:

$$\lambda_3 = -\frac{I_0}{\sigma_0^2}\left(\frac{x-R}{x}\right)$$

$$\lambda_2 = -\frac{I_0}{\sigma_0^2}\left[1 - \left(\frac{CM}{\sigma_0}\right)^2\right]$$

$$\lambda_1 = -\frac{I_0}{\sigma_0^2}$$

B Eigenvalues for a cylindrical model with elliptical section

The elliptical section is defined by one standard deviation along the x axis: σ_x and one standard deviation along the y axis: σ_y. The model is then defined by:

$$I_0(x,y,z) = Ce^{-\frac{1}{2}\left[\left(\frac{x}{\sigma_x}\right)^2+\left(\frac{y}{\sigma_y}\right)^2\right]}$$

The Hessian matrix can be expressed as

$$H = \frac{I_0(x,y,z)}{\sigma_x^2\sigma_y^2}H'$$

where H' is expressed as:

$$\begin{bmatrix} \sigma_y^2\left(X^2-1\right) & \sigma_x\sigma_y XY & 0 \\ \sigma_x\sigma_y XY & \sigma_x^2\left(Y^2-1\right) & 0 \\ 0 & 0 & 0 \end{bmatrix} = \begin{bmatrix} E & F & 0 \\ F & G & 0 \\ 0 & 0 & 0 \end{bmatrix}$$

with $X = \frac{x}{\sigma_x}$ and $Y = \frac{y}{\sigma_y}$.

The determinant of $H' - \lambda Id$ is

$$\begin{aligned} det &= -\lambda\left[\lambda^2 - \lambda\left(E+G\right) + EG - F^2\right] \\ &= -\lambda\left[\begin{array}{l} \lambda^2 - \lambda\left(\sigma_y^2X^2 + \sigma_x^2Y^2 - \sigma_x^2 - \sigma_y^2\right) \\ +\sigma_x^2\sigma_y^2\left(1 - X^2 - Y^2\right) \end{array}\right] \end{aligned}$$

Let $P(\lambda) = \lambda^2 - \lambda\left(E+F\right) + EF - G^2$,

the determinant of P is

$$\begin{aligned} \Delta &= (E+G)^2 - 4(EG - F^2) \\ &= (E-G)^2 + 4F^2 > 0 \text{ if } \sigma_x \neq \sigma_y \end{aligned}$$

$$\lambda_1 = \frac{1}{2}(E+G-\sqrt{\Delta}) \quad ; \quad \lambda_2 = \frac{1}{2}(E+G+\sqrt{\Delta})$$

The expression of the eigenvalues is $\frac{1}{2}(E+G\pm\sqrt{(E+G)^2+4(F^2-EG)})$ where $F^2-EG = \sigma_x^2\sigma_y^2\left[(\frac{x}{\sigma_x})^2+(\frac{y}{\sigma_y})^2-1\right]$. We can then distinguish three cases depending on the position of $M(x,y)$, expressed in table 1. We can also study the eigenvalues along the x and y axis. In both cases, $F = 0$ and H' is diagonal so $\vec{\mathbf{v}}_\mathbf{1} = (1,0,0)$ and $\vec{\mathbf{v}}_\mathbf{2} = (0,1,0)$, the result is given in table **??**

$$\vec{\mathbf{v}}_i = \begin{pmatrix} \lambda_i - G \\ F \\ 0 \end{pmatrix} = \begin{pmatrix} F \\ \lambda_i - E \\ 0 \end{pmatrix} \quad \text{for} \;\; i \in \{1, 2\}.$$

C Expression of the maximal scale depending on γ

We want to detect the axis of the vessel which is defined by $x = y = 0$. The response at a point $M(0, 0, z)$ is given by:

$$R_t(\bar{x}) \;=\; \frac{1}{2\theta\pi\sqrt{t}} \int_{\bar{x} \in C_{\theta\sqrt{t}}} |\nabla L(\bar{x}, t).\vec{n}| \, d\bar{x}$$

which corresponds to the mean of the vector product of the gradient with the unit radial vector along the circle of center $(0, 0, z)$ and of radius $\theta\sqrt{t}$. The gradient and the normal vector $\vec{n}$ have the following expressions:

$$\nabla L(\bar{x}, t) = L(\bar{x}, t) \frac{-1}{t + \sigma_0^2} \begin{pmatrix} x \\ y \\ 0 \end{pmatrix}$$

$$\vec{n} = \frac{1}{\sqrt{x^2 + y^2}} \begin{pmatrix} x \\ y \\ 0 \end{pmatrix} \text{ with } x^2 + y^2 = \theta^2 t$$

then

$$|\nabla L(\bar{x}, t).\vec{n}| = C \frac{\theta\sqrt{t}}{2\pi\, (t + \sigma_0^2)^2} \; e^{-\frac{\theta^2 t}{2(t + \sigma_0^2)}}$$

This last expression is no longer a function of $\bar{x}$, then the mean of this expression along the circle is straightforward, and

$$R_t \quad = \quad C \frac{\theta\sqrt{t}}{2\pi\, (t + \sigma_0^2)^2} \; e^{-\frac{\theta^2 t}{2(t + \sigma_0^2)}}$$

The normalized response R_t^n is defined by $R_t^n \;=\; t^{\gamma/2} R_t$ and its partial derivative on t is:

$$\frac{\partial R_t^n}{\partial t} \quad = \quad A \frac{C t^{\frac{\gamma - 1}{2}}}{4\pi\, (t + \sigma_0^2)^4} e^{-\frac{\theta^2 t}{2(t + \sigma_0^2)}}$$

$$\text{with } A = (\gamma - 3)t^2 + (2\gamma - 2 - \theta^2)\, \sigma_0^2\, t + (1 + \gamma)\sigma_0^4.$$

We are looking for the value of γ which gives a maximum for the function R_t^n at $t = \sigma_0^2$. Thus we want $\frac{\partial R_t^n}{\partial t}$ to have a positive root which corresponds to a maximum.

The sign of $\frac{\partial R_t^n}{\partial t}$ is the same as the sign of A, and the expression A, when $\gamma < 3$ and the determinant Δ is also positive, has only one positive root which corresponds to a maximum for R_t^n :

$$h(\gamma, \theta) = \frac{\sqrt{\Delta} - 2\gamma + 2 - \theta^2}{2(3 - \gamma)}$$

with

$$\Delta = \left[\theta^2 - (2\gamma - 2)\right]^2 + 16 - (2\gamma - 2)^2.$$

References

[Blu67] H. Blum. A transformation for extracting new descriptors of shape. In W. Wathe-Dunn, editor, *Models for the perception of Speech and Visual Form*, pages 363–380, MIT Press, Cambridge, 1967.

[BM94] G. Bertrand and G. Malandain. A new characterization of three-dimensional simple points. *Pattern Recognition Letters*, 15(2):169–175, February 1994.

[BN78] H. Blum and R.N. Nagel. Shape description using weighted symmetric axis features. *Pattern Recognition*, 10:167–180, 1978.

[Del94] H. Delingette. Intrinsic stabilizers of planar curves. In *3rd European Conference on Computer Vision (ECCV'94)*, Stockholm, Sweden, June 1994.

[EGMP94] D. Eberly, R. Gardner, B. Morse, S. Pizer, and C. Scharlach. Ridges for image analysis. *Journal of Mathematical Imaging and Vision*, 4:353–373, 1994.

[FEPM95] D. S. Fritsch, D. Eberly, S. M. Pizer, and M. J. McAuliffe. Simulated cores and their application in medical imaging. *Information Processing in Medical Imaging*, 365–368, 1995.

[Fid97] Márta Fidrich. Following feature lines across scale. In *Scale-Space Theory in Computer Vision*, pages 140–151, Springer-Verlag, Utrecht, July 1997.

[FKMP97] J.D. Furst, R.S. Keller, J.E. Miller, and S.M. Pizer. Image loci are ridges in geometric spaces. In *First Intern Conf on Scale-Space Theory in Computer Vision*, Utrecht, July 1997.

[FP98] J.D. Furst and S.M. Pizer. *Marching Optimal-Parameter Ridges: an Algorithm to Extract Shape Loci in 3D Images.* Technical Report TR-98-006, University of North Carolina, 1998.

[FPE96] J.D. Furst, S.M. Pizer, and D. Eberly. Marching cores: a method for extracting cores from 3d medical images. In *Proc. Workshop on Math. Methods in Biomed. Image Anal.*, pages 124–130, 1996.

[FPME94] D.S. Fritsch, S. M. Pizer, B. S. Morse, D.H. Eberly, and A. Liu. The multiscale medial axis and its applications in image registration. *Pattern Recognition Letters*, 15(5):445–452, 1994.

[Fra98] F. Frangi. Multiscale vessel enhancement filtering. In William M. Wells Alan Colchester Scott Delp, editor, *Lecture Notes in Computer Science, MICCAI'98*, pages 130–137, October 1998.

[FtHRKM92] L.M. Florack, B.M. ter Haar Romeny, J.J. Koenderink, and Viergever M.A. Scale and the differential structure of images. *Image and Vision Computing*, 10(6):376–388, July 1992.

[KGSD95] T.M. Koller, G. Gerig, G. Székely, and D. Dettwiler. Multiscale detection of curvilinear structures in 2D and 3D image data. In IEEE, editor, *International Conference on Conputer Vision (ICCV'95)*, pages 864–869, 1995.

[KMA98] K. Krissian, G. Malandain, and N. Ayache. *Model Based Multiscale Detection and Reconstruction of 3D Vessels.* Technical Report 3442, INRIA Sophia Antipolis, 2004 route des Lucioles BP 93 06902 Sophia Antipolis Cedex (France), June 1998.

[KMAV98a] K. Krissian, G Malandain, N. Ayache, R. Vaillant, and Y. Trousset. Model-based multiscale detection of 3d vessels. In *Computer Vision and Pattern Recognition*, pages 722–727, June 1998.

[KMAV98b] K. Krissian, G Malandain, N. Ayache, R. Vaillant, and Y. Trousset. Model-based multiscale detection of 3d vessels. In Baba Vemuri, editor, *Workshop on Biomedical Image Analysis*, pages 202–208, Santa Barbara, 1998.

[Koe84] J. J. Koenderink. The structure of images. *Biol. Cybern.*, 50(363-370), 1984.

[LC87] W.E. Lorensen and H.E. Cline. Marching cubes: A high resolution 3-D surface construction algorithm. *Computer Graphics*, 21(4):163–169, 1987.

[LCBF97] C. Lorenz, I.-C. Carsen, T.M. Buzug, C. Fassnacht, and J. Weese. Multi-scale line segmentation with automatic estimation of width, contrast and tangential direction in 2d and 3d medical images. In *CVRMed-MRCAS'97*, pages 213–222, Grenoble, France, March 1997. Lecture notes in Computer Science 1205, Springer Verlag.

[Lin94] T. Lindeberg. *Scale-Space Theory in Computer Vision.* Kluwer Academic Publishers, Dordrecht, Netherlands, 1994.

[Lin96] T. Lindeberg. Edge detection and ridge detection with automatic scale selection. In *IEEE Comp. Soc. Conf. on Computer Vision and Pattern Recognition*, page 465, San Francisco, June 1996.

[MPL94] B.S. Morse, S.M. Pizer, and A. Liu. Multiscale medial analysis of medical images. *Image and Vision Computing Volume*, 12(6):327–338, July/August 1994.

[Pay96] Etienne Payot. *Reconstruction Vasculaire tridimensionnelle en imagerie par rayons X.* Ph.D. dissertation, Ecole Nationale Supérieure des Télécommunication, 1996.

[PBCF94] S.M. Pizer, C.A. Burbeck, J.M. Coggins, D.S. Fritsch, and B.S. Morse. Object shaphe before boundary shape: Scale-space medial axes. *Journal of Mathematical Imaging and Vision*, 4:303–313, 1994.

[PEFM98] S.M. Pizer, D. Eberly, D. Fritsch, and B.S. Morse. Zoom-invariant vision of figural shape: The mathematics of cores. *Computer Vision and Image Understanding*, 69(1):55–71, January 1998.

[SNAK97] Y. Sato, S. Nakajima, H. Atsumi, T. Koller, G. Gerig, S. Yoshida, and R. Kikinis. 3d multiscale line filter for segmentation and visualization of curvilinear structures in medical images. In *CVRMed-MRCAS'97*, pages 213–222, March 1997. Lecture Notes in Computer Science 1205, Springer Verlag.

[SNSA98] Y. Sato, S. Nakajima, N. Shiraga, H. Atsumi, S. Yoshida, T. Koller, G. Gerig, and R. Kikinis. Three-dimensional multi-scale line filter for segmentation and visualization of curvilinear strutures in medical images. *Medical Image Analysis*, 2(2):143–168, June 1998.

[TG92] J.P. Thirion and A. Gourdon. *The 3D marching lines algorithm and its application to crest lines extraction.* Technical Report RR-1672, INRIA, Sophia-Antipolis, 1992.

[TG93] J.P. Thirion and A. Gourdon. *The marching lines algorithm:New results and proofs.* Technical Report RR-1881-1, INRIA, Sophia-Antipolis, 1993.

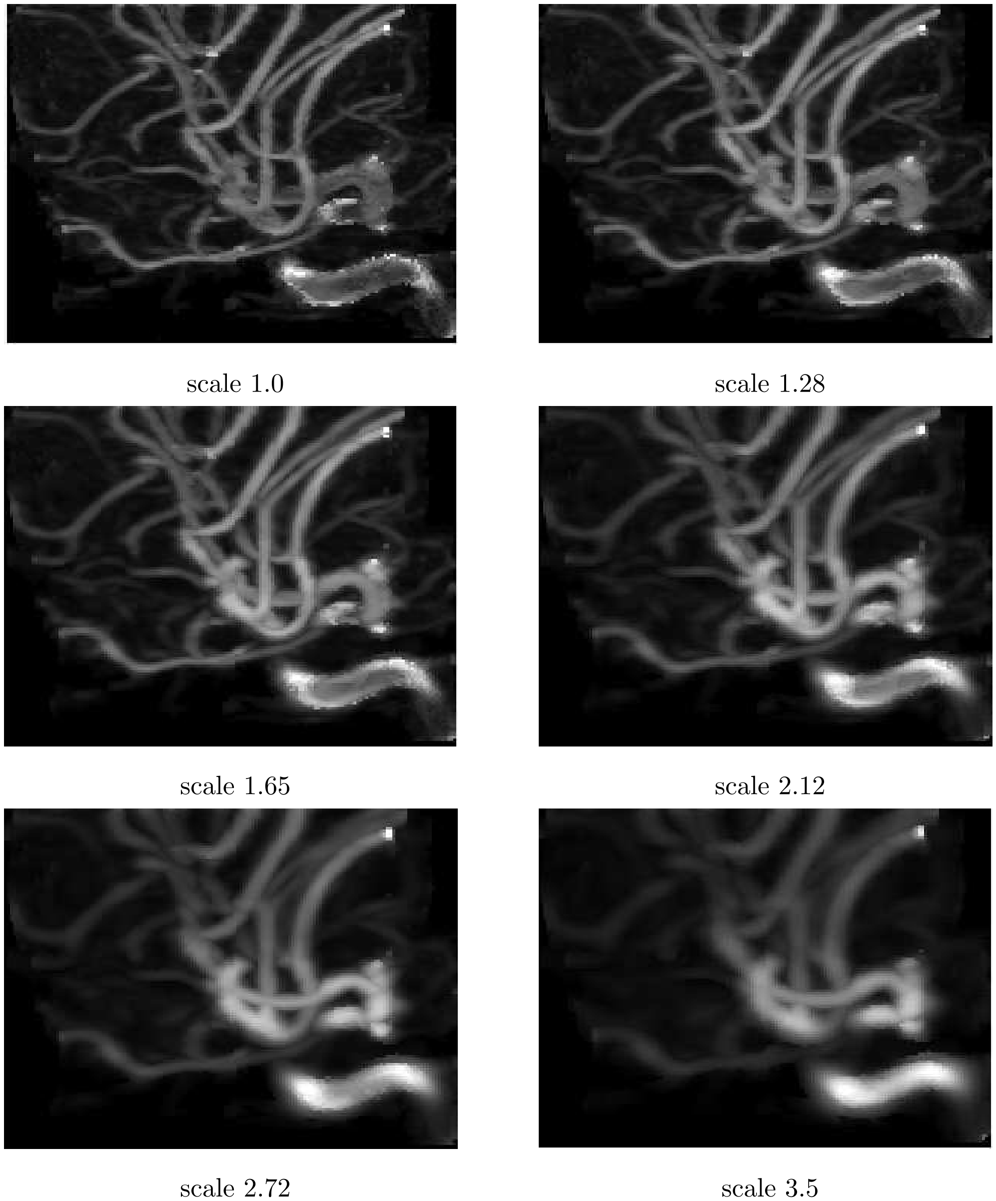

Figure 5: MIP views of the responses obtained for 6 scales.

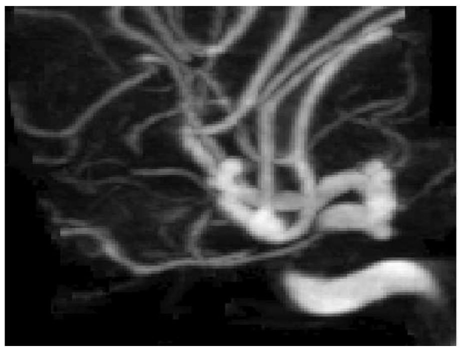

initial image

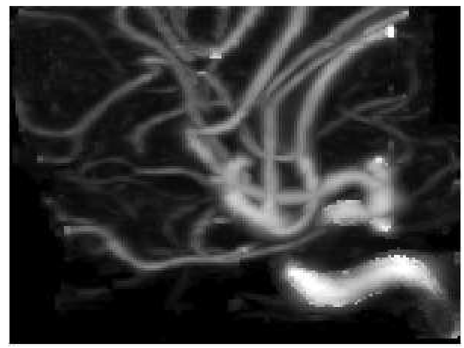

maximum response across scales

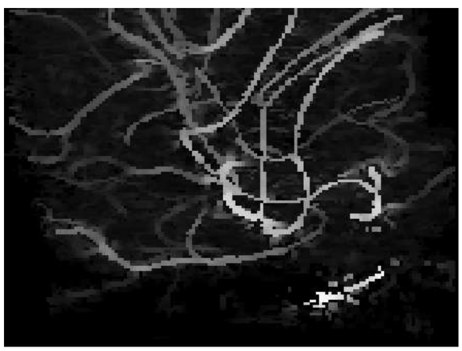

local extrema from the maximum response

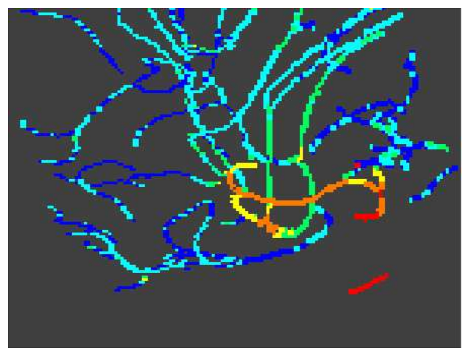

center of the vessels with colors depending on the detected scale.

Color						
Scale	1.0	1.28	1.65	2.12	2.72	3.5

Figure 6: Maximum Intensity Projections at different stages of the multiscale analysis.

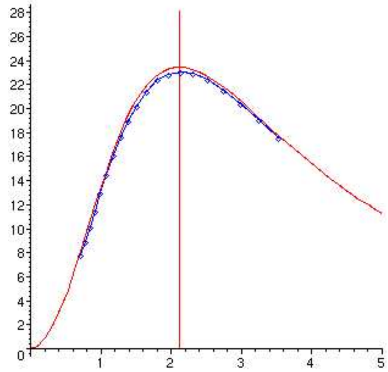

Figure 7: Response obtained at the center of the vessel for different scales. In red, the theoretical profile, and in blue the obtained profile. The vertical line shows the theoretical scale for which the response is maximal.

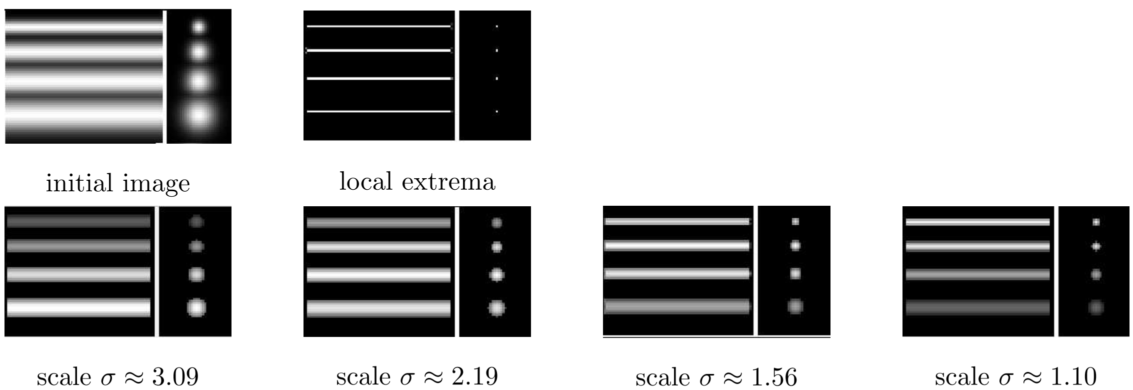

Figure 8: cylinder with circular Gaussian cross-section. Responses obtained for the optimal scales.

real vessel radius	1.25	1.75	2.5	3.5
maximum intensity	20.8085	22.3763	22.7294	22.9052
distance to theoretical value	10.8667%	4.1510%	2.6385%	1.8855%
estimated radius	1.55	1.79	2.58	3.46
error in voxels	0.3	0.04	0.08	0.04

Table 3: intensity obtained at the center of the vessels for a range of 10 scales, estimated sizes and error in the estimation.

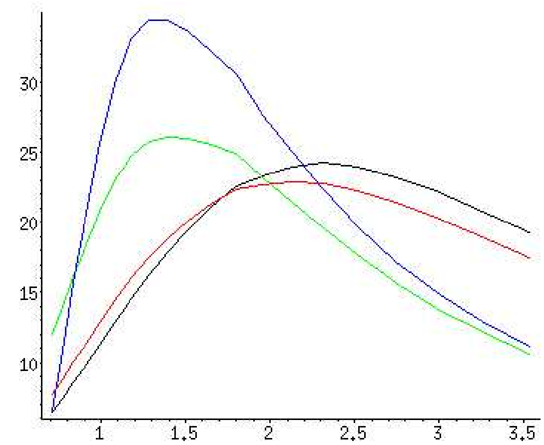

Figure 9: Response profiles obtained for a Gaussian-like cross-section in red, for a bar-like cross-section in blue, for a bar-like cross-section convolved with a Gaussian $\sigma = 1$ in green, for a bar-like cross-section convolved with a Gaussian $\sigma = 3$ in black,

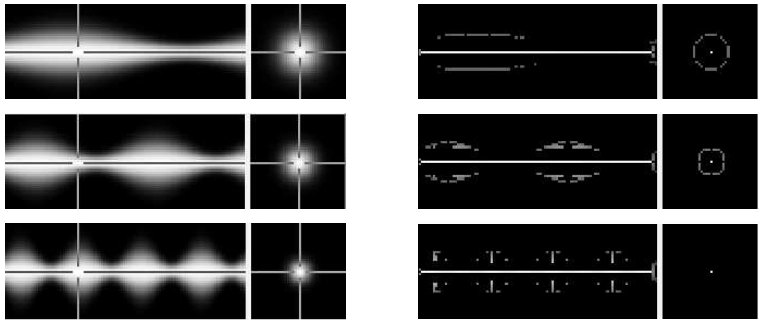

synthetic images local extrema

Figure 10: Tests on an Gaussian cross-section vessel with varying radius.

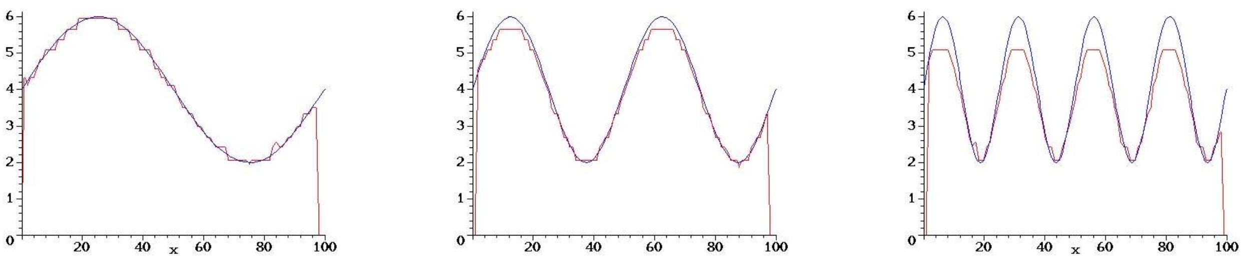

n=1 n=2 n=4

Figure 11: Comparison of the real and the detected radii along z axis.

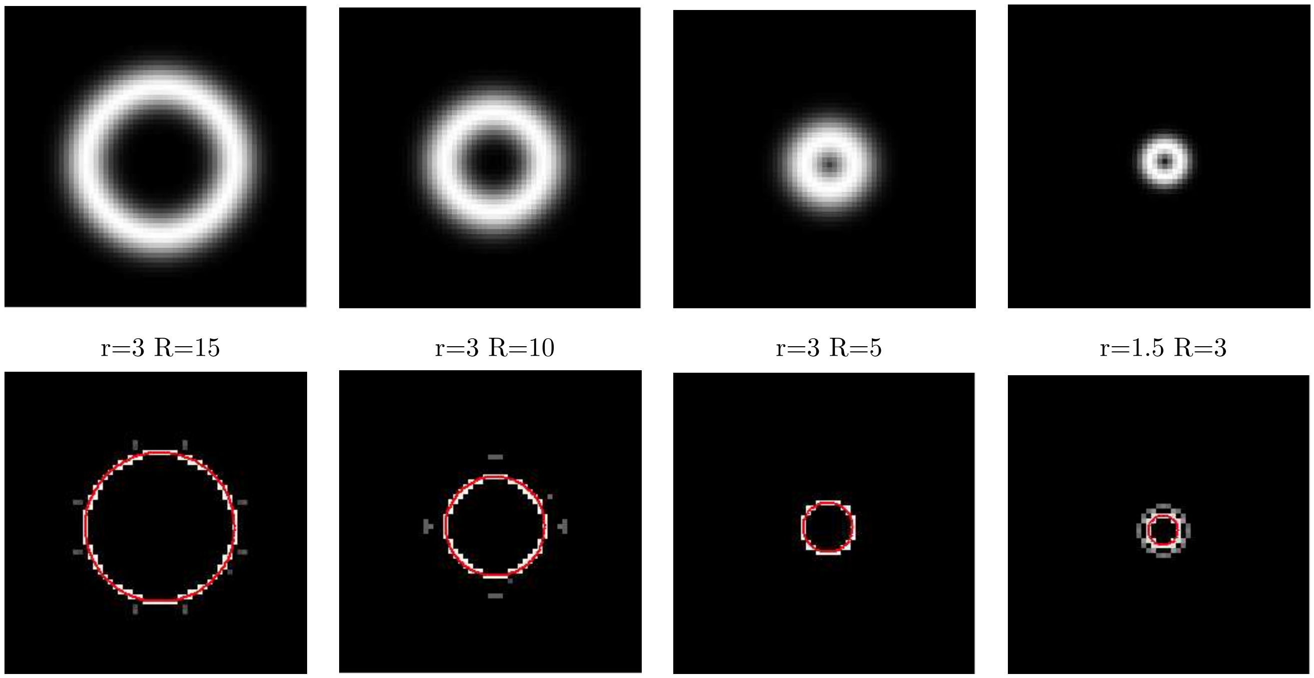

Figure 12: Detection of torus with Gaussian cross-section and different curvatures. At the top, MIPs of the initial images; At the bottom, comparison of the images of local maxima and the real center axis in red.

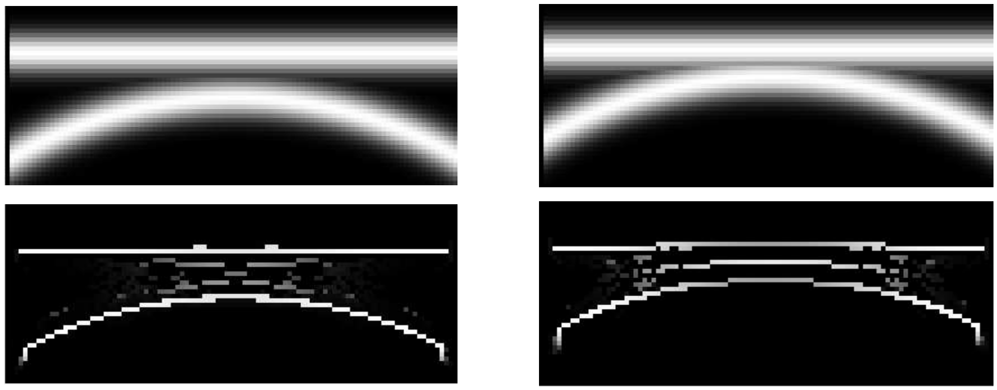

$d = 3$ voxels $d = 0$

Figure 13: Tangent vessel, tangency parallel to the vessel axis ($\alpha = 0$).

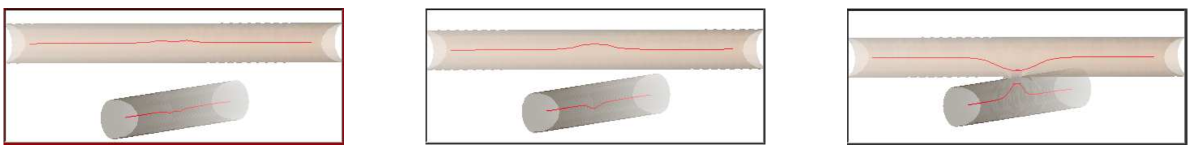

$d = 4$ voxels $d = 2$ voxels $d = 0$

Figure 14: Tangent vessels, tangency orthogonal to the vessel axis ($\alpha = \pi/2$).

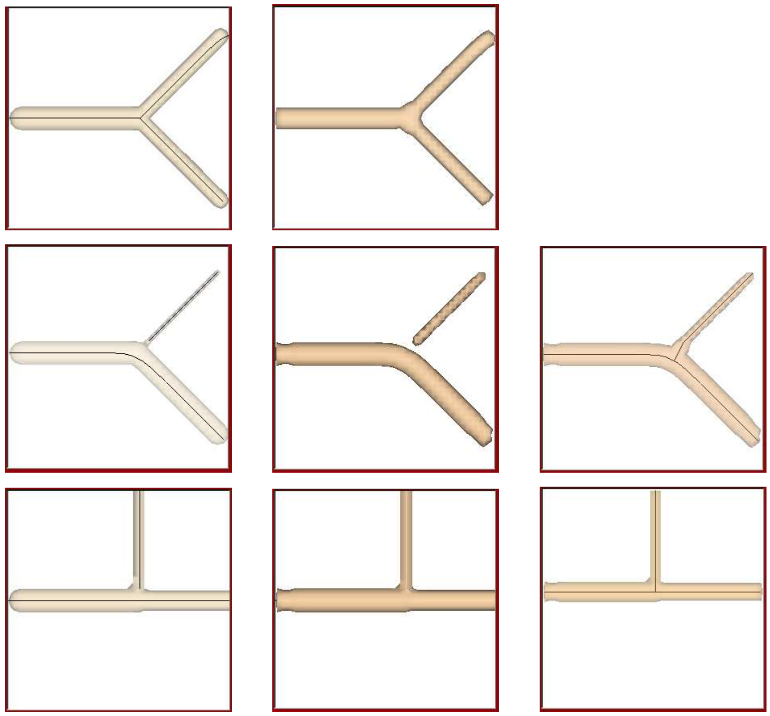

Figure 15: Centerlines detection and reconstruction on three synthetic junction images. Left, initial image and the detected centerlines. Middle, reconstruction before junction connection. Right, centerlines and reconstruction after junction connection.

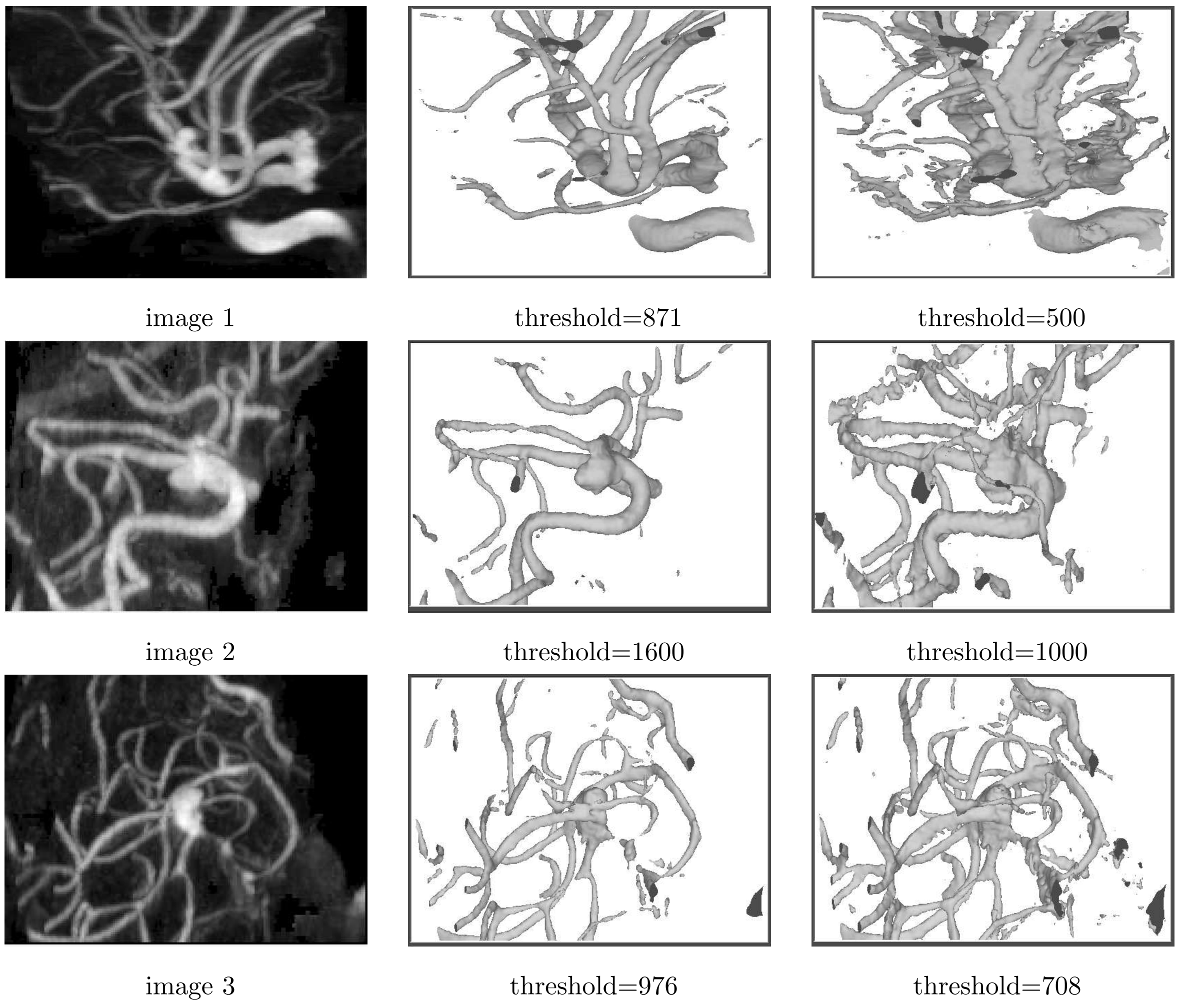

Figure 16: Top, MIP view and isosurfaces of the initial image. Bottom, centerlines and reconstruction.

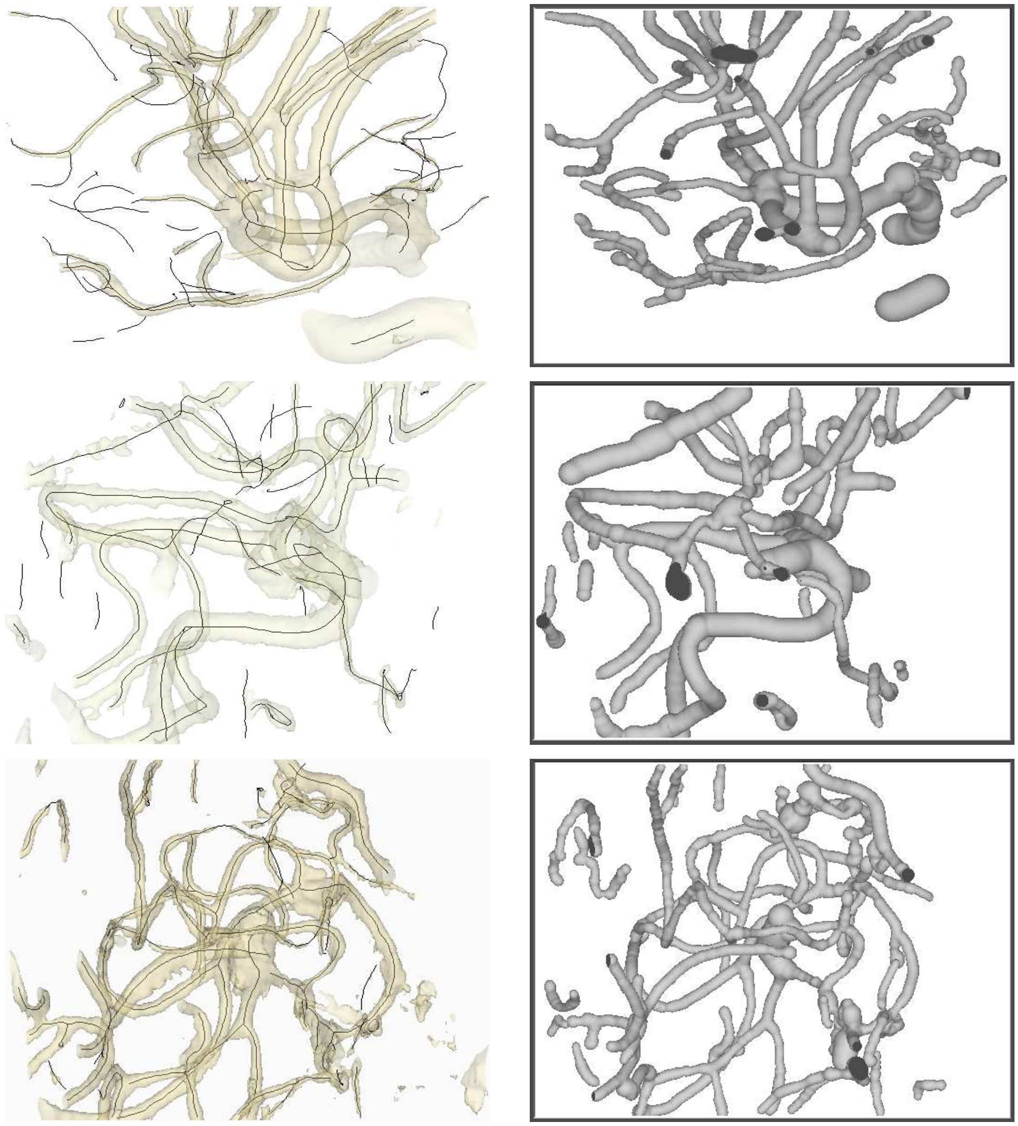

Figure 17: Results on the images represented in Fig. 16. Left, detected centerlines superimposed on an isosurface of the initial image. Right, reconstruction of the vessels network from centerlines and radii estimation.

Figure 18: Initial MRA Image.

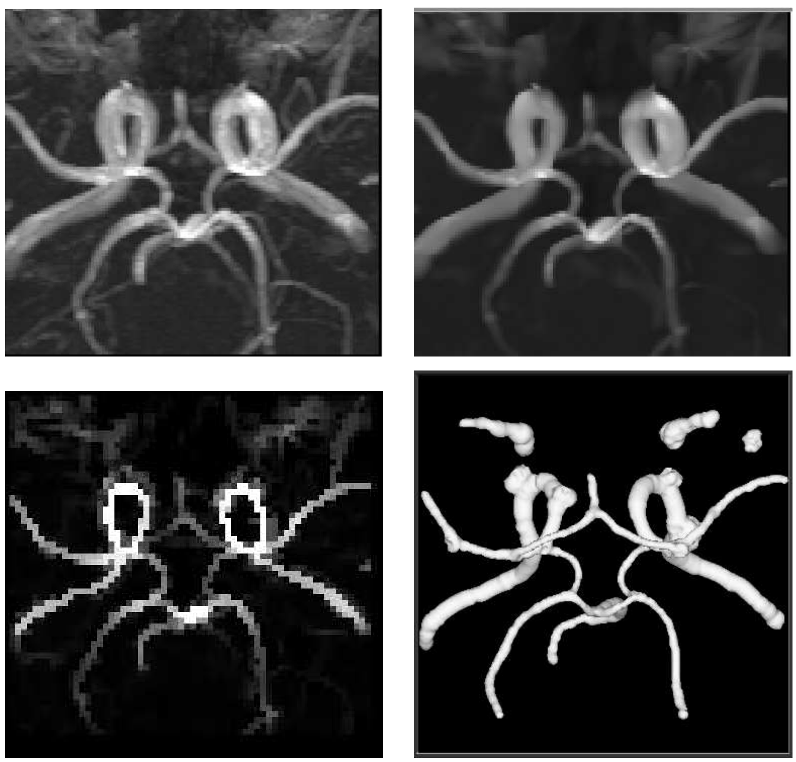

Figure 19: MIP of a sub-image on the top left and the resulting image after anisotropic filtering on the top right. Bottom left, image of the local extrema; and bottom right, vessels reconstruction.